RESEARCH ARTICLE

Stereoscopic PIV measurements of flow in the nasal cavity with high flow therapy

C. J. T. Spence · N. A. Buchmann ·
M. C. Jermy · S. M. Moore

Abstract Knowledge of the airflow characteristics within the nasal cavity with nasal high flow (NHF) therapy and during unassisted breathing is essential to understand the treatment's efficacy. The distribution and velocity of the airflow in the nasal cavity with and without NHF cannula flow has been investigated using stereoscopic particle image velocimetry at steady peak expiration and inspiration. In vivo breathing flows were measured and dimensionally scaled to reproduce physiological conditions in vitro. A scaled model of the complete nasal cavity was constructed in transparent silicone and airflow simulated with an aqueous glycerine solution. NHF modifies nasal cavity flow patterns significantly, altering the proportion of inspiration and expiration through each passageway and producing jets with in vivo velocities up to 17.0 ms^{-1} for 30 l/min cannula flow. Velocity magnitudes differed appreciably between the left and right sides of the nasal cavity. The importance of using a three-component measurement technique when investigating nasal flows has been highlighted.

C. J. T. Spence (✉) · M. C. Jermy · S. M. Moore
Centre for Bioengineering, Department of Mechanical
Engineering, University of Canterbury, Private Bag 4800,
Christchurch 8041, New Zealand
e-mail: callumjts@gmail.com

N. A. Buchmann
Laboratory for Turbulence Research in Aerospace
and Combustion, Department of Mechanical
and Aerospace Engineering, Monash University,
Melbourne, VIC 3800, Australia

1 Introduction

Nasal cannulae are used to administer a breathing ventilation therapy known as nasal high flow (NHF). NHF produces elevated airway pressures (Groves and Tobin 2007; Locke et al. 1993) to help treat patient conditions such as chronic obstructive pulmonary disease (COPD) and hypoxic pneumonia. For a given cannula flow rate, because everyone's anatomy is different, everyone experiences a different airway pressure and therefore level of therapy. To better understand the therapy, it is necessary to understand the flow phenomena in the nasal cavity associated with NHF and how elevated pressures are generated. In this study, the flow velocities in the nasal cavity with and without NHF flow have been mapped in vitro using stereoscopic particle image velocimetry (SPIV). As well as elucidating the effect of NHF flow in the nasal cavity, the results contribute to the understanding of the flow in the nasal cavity during unassisted breathing by providing the flow pattern in another unique geometry. Interpersonal variation of nasal cavity geometry is wide, and it is important to confirm that results from the limited number of geometries investigated in other studies are applicable to the general population.

1.1 Breathing therapies

Cannulae therapy until recently has been limited to low flow rates due to the discomfort and irritation caused by delivering dry, cold gas to the nasal passages (Campbell et al. 1988). NHF, however, delivers heated and humidified air at body temperature pressure saturated (BTPS) to patients at steady flows ranging from 5 to 50 l/min via a nasal cannula. BTPS air is 37°C, has a relative humidity of 100% and an absolute humidity of 43.9 mg H_2O/l. The

Fig. 1 Optiflow^{TM} nasal cannula produced by Fisher & Paykel Healthcare

Optiflow^{TM} nasal cannula (Fig. 1) investigated in this study is produced by Fisher & Paykel Healthcare, Auckland, New Zealand, and consists of a manifold that rests on the upper lip and two elliptical cross-section prongs, which have mean diameter of 5 mm and protrude into each nostril by approximately 10 mm.

NHF has advantages over conventional methods. High continuous flow rates reduce the dilution of oxygen (Gibson et al. 1976) and anatomical dead space, delivering higher oxygen fractions (Lund et al. 1996). The use of nasal and full-face continuous positive airway pressure (CPAP) masks is well established; however, it has been reported that NHF has greater patient compliance (Sreenan et al. 2001) because it is more comfortable and allows patients to drink, eat and communicate without interruption of the therapy. NHF provides ventilation with or without supplemental oxygen. Humidification prevents dehydration and thickening of secretions (Conway et al. 1992) and subsequent irritation of the nasal mucosa. For these reasons, NHF is also used to treat patients with impaired saliva glands undergoing head and neck cancer radiotherapy or in postoperative recovery.

In order for clinicians to make informed decisions on NHF flow rates, it is necessary to understand the effect of the nasal cannula airflow on the flow velocity distribution and magnitude in the nasal cavity. SPIV velocimetry was therefore chosen for its ability to accurately measure complex three-dimensional flow fields.
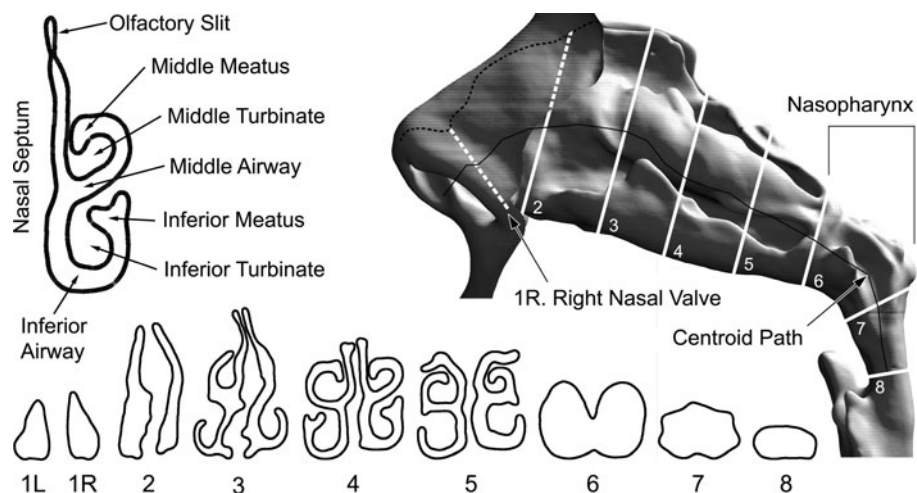
1.2 Nasal cavity geometry

The nasal cavity has tortuous passages that form a large surface area and are lined with mucosa. These moist surfaces are extensively vascularised and facilitate the mechanism for heat transfer and evaporation of water from mucus. The nasal cavity begins at the nasal vestibule and extends backward as two separate airways partitioned by the nasal septum (Fig. 2), until the nasopharynx where the airways merge. The nasal vestibule is the area enclosed by the external cartilages of the nose and is lined with small, filtering hairs. The turbinates (or concha) are long, narrow and curled bone shelves that protrude into the nasal cavity, creating a large surface area and forming the inferior, middle and superior airways and meatus passageways. The olfactory receptors, responsible for the sense of smell, are located in the olfactory slit on the nasal cavity roof.

The nasal valve occurs just posterior of the nasal vestibule and is the region of smallest cross-sectional area. The nasal valves for the in vitro model used in this study can be seen as the curve minima labelled 1L and 1R in Fig. 3 and have cross-sectional areas of 1.11 and 1.15 cm^2, respectively. These cross-sectional areas lie within the 0.54–1.21 cm^2 range measured by Çakmak et al. (2003) using CT data from 25 healthy adults. The size of the nasal valve is not static but constantly changing with surrounding erectile tissues (Cole 2000) inflating and deflating during the nasal cycle. Following the nasal valve is an abrupt expansion into the main cavity both in height and in cross-sectional area. Although each side of the nasal cavity shares common features, they are asymmetric. The cross-sectional area of the right nasal cavity 7.2 cm posterior of the external naris (nostrils) was 30% larger than on the left. Liu et al. (2009) in pursuing an average geometry of the human nasal cavity obtained CT scans of 30 healthy subjects that had been confirmed to have nasal anatomy within normal limits and found the internal volume of the middle

Fig. 2 Coronal cross sections of a 44-year-old male's nasal cavity with respective locations illustrated on the sagittal view

Fig. 3 Variations of the cross-sectional area through the nasal cavity versus distance along a centroid path (Fig. 2) measured from the external naris. The *numbered* locations correspond to those illustrated in Fig. 2
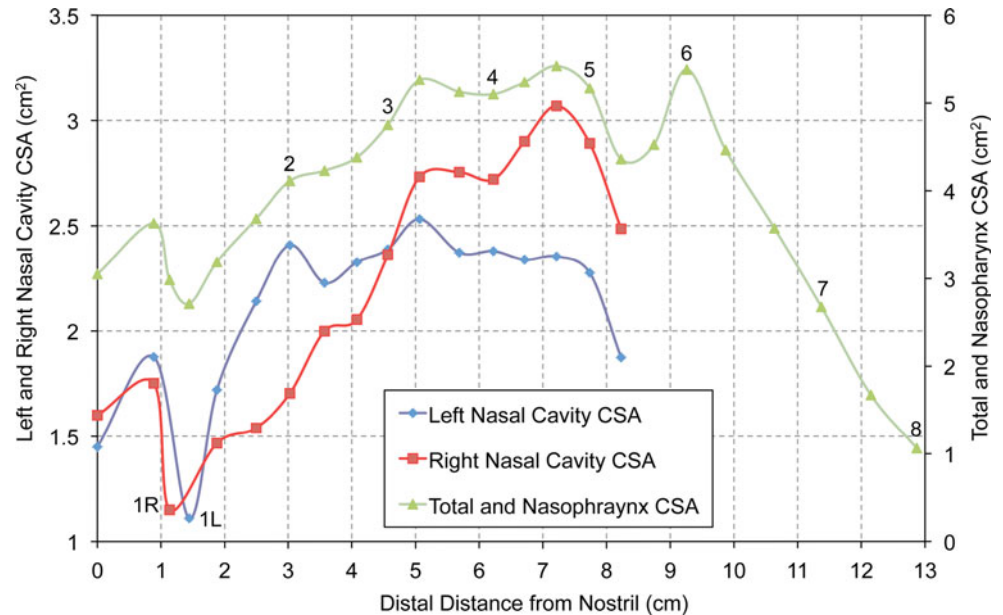
region of the left and right nasal cavities to vary by up to 65%. A high degree of asymmetry in the left and right passages of healthy adults was therefore considered to be normal.

Beyond the nasal cavity, the cross-sectional area narrows through the nasopharynx before reaching a minimum cross-sectional area of 1.1 cm^2 in the oropharynx, which is shown as location 8 in Figs. 2 and 3. The size of the oropharynx is dependant on the position of the soft palette. The soft palette is the muscle tissue that forms the back roof of the mouth and will be either closing off the oral cavity during nasal breathing, closing off the nasal passages during mouth breathing, or in a neutral position. The soft palette in the current study's geometry occluded the oral cavity and notably created a smaller airway than the combined cross sections of the two nasal valves.

1.3 Nasal cavity airflow measurements

In vivo studies of the flow pattern within the nasal cavity are prevented by the complex geometry and inaccessibility of the nasal passageways. In vitro measurement of nasal cavity flow requires the use of artificial nasal models. The procedure for creating physiologically accurate models from non-invasive medical imaging is now well established, using methods built on the procedure presented by Hopkins et al. (2000).

Wolf et al. (2004) gave a survey of knowledge at the time on the air-conditioning and flow characteristics of the human nose obtained from experimental and computational methods. Wolf et al. (2004) described the air to enter the nostrils and rise vertically along the bridge towards the

anterior end of the middle turbinate. On inspiration, maximum velocities of 6–18 ms^{-1} were measured at the nasal valve, decreasing to 2 ms^{-1} in the main passage and increasing again to 3 ms^{-1} in the nasopharynx. A large proportion of the flow was found to pass through the middle airway. During expiration, maximum velocities of 3–6 ms^{-1} were measured in the nasal valve, with an evenly distributed velocity of 1–2 ms^{-1} throughout the nasal cavity.

Planar particle image velocimetry (PIV) has been used in a number of studies to measure nasal flow structures in transparent models using a refractive index–matched water–glycerol working fluid mixture. PIV measurements (Hopkins et al. 2000) confirmed on inspiration a standing eddy in the region posterior to the nasal valve caused by the adverse pressure gradient along the abrupt expansion in cross-sectional area. Both Kelly et al. (2000) and Kim et al. (2006) reported laminar flow streams through the middle airway, high velocities in the nasal valve and inferior airway and low velocities in the olfactory region. Doorly et al. (2008) provided a recent review of PIV studies in the nasal cavity and described the emergence of a jet from the internal nasal valve into the main cavity on inspiration.

The current paper, to the authors' knowledge, describes the first reported SPIV nasal cavity velocity maps, with or without assisted ventilation flows and in a flow phantom that includes both sides of the nasal cavity. The methodology of model construction and of the SPIV measurements are described. Flow patterns at steady flow during unassisted breathing and with NHF flow are shown. In vitro flow conditions were dimensionally scaled from preliminary in vivo breath flow measurements.
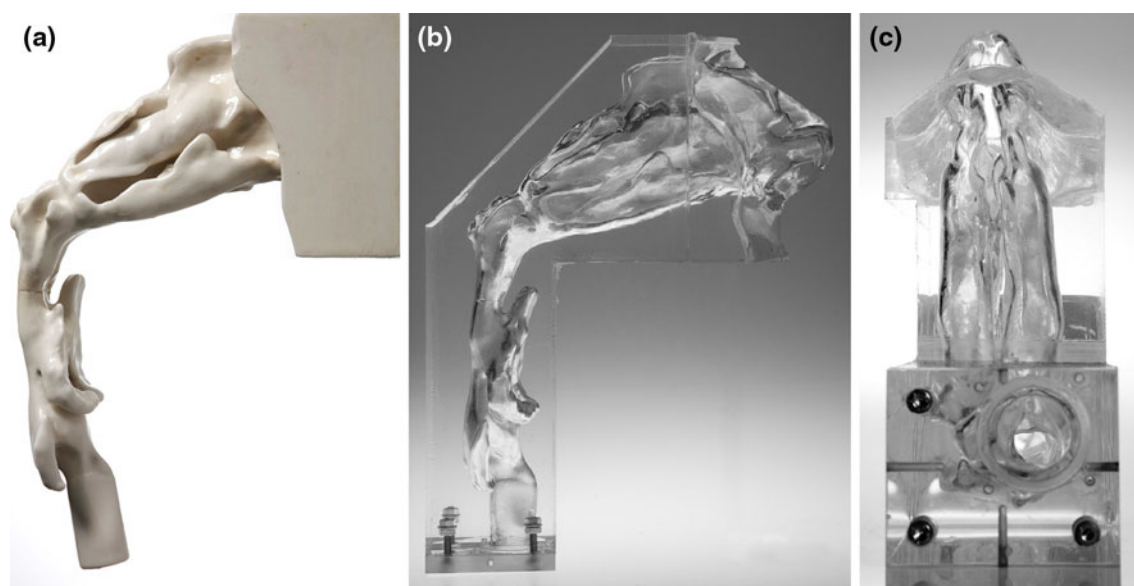
Fig. 4 a Nasal cavity rapid prototyped geometry and **b** silicone nasal cavity flow phantom viewed sagittally from the *left* and **c** axially from the *bottom*

2 Experimental method

2.1 Nasal cavity flow phantom

A 1.55 times scale flow phantom of a complete human nasal cavity was constructed employing medical computed tomography (CT) scan data and rapid prototyping. The CT data set of an anonymous 44-year-old man comprised 452 axially acquired 512×512 pix^2 resolution images with a 0.6-mm slice spacing and thickness. A radiologist declared the nasal cavity free of any visible abnormalities. The respiratory tract surface geometry was extracted from the CT data using in-house software combining the ITK (http://www.itk.org) and VTK (http://www.vtk.org) frameworks into an interactive image segmentation package. The surface extraction algorithm used was the 'vtkContourFilter', analogous to the Marching Cube algorithm of William and Harvey (1987). The resolution and contrast of the CT scan were sufficiently high to negate the use of level set methods for segmentation. A circular cross section lofted to the termination of the trachea to facilitate the connection of the phantom to flow conduits.

The geometry was rapid prototyped (Fig. 4a) in a water dissoluble material and embedded in a clear silicone resin. After the silicone resin had cured, the model was removed, leaving a transparent scaled flow phantom of the nasal cavity (Fig. 4b). Both sides of the nasal cavity and trachea termination are visible in Fig. 4c. The flow entering the nostrils is influenced by the shape of the external nose and was therefore included in the phantom. Physiological features such as nostril hairs and mucous membranes inside the nasal cavity were not resolved because the main interest of this paper was the large- and medium-scale flow features, which were assumed independent of these details. As with all other PIV measurements of nasal cavity flows to date, the sinuses were assumed to have negligible effect on the airflow because the openings to the sinuses (ostia) are very small and were excluded from consideration to reduce optical noise. The cannula was rapid prototyped in clear stereo-lithography resin with a refractive index of 1.51. Reflections from the cannula were, however, minimised by painting the cannula models matt black.

2.2 Flow system

The nasal cavity phantom was installed in a recirculating flow system as shown in Fig. 5. A constant pressure header tank supplied steady expiration and cannula flows, and steady flow was pumped in reverse for inspiration. The physiological geometry upstream of the nasal cavity and the abrupt changes in flow direction within the cannula manifold negated the use of fully developed inlets. Two electromagnetic flow meters (Tigermag FM626, Krohne IFC 010D) and valves were used to adjust the individual cannula and throat flow rates. Return and overflow lines connected the reservoir and header tank to ensure flow over the weir and constant head.

A mixture of water and glycerine was used as a working fluid to match the refractive index of the flow phantom. The refractive index of the silicone rubber used for the phantom construction is specified as 1.43 by the manufacturer, which varies due to differences in mixing and

Fig. 5 Schematic of the experimental set-up
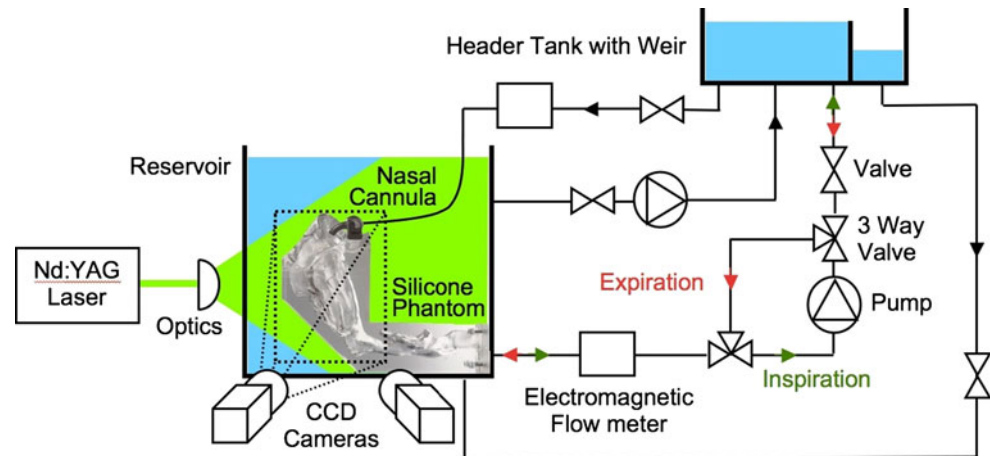
curing from model to model. The optimum mixture was found to be 39% water and 61% glycerine by volume. The phantom was immersed in the reservoir to a depth such that the free surface remained flat at the highest flow rate, effectively providing a constant pressure at the nostrils.

To ensure physiologically accurate flow rates were reproduced in vitro, preliminary in vivo measurements were conducted and subsequently dynamically scaled. Results have shown that NHF modifies natural inspiratory and expiratory flow rates and breathing frequencies by assisting inspiration and providing resistance on expiration. Peak inspiration and expiration flow rates with NHF were measured in vivo on a healthy 23-year-old man with height 184 cm and weight 85 kg. To quantify the leakage flow rate between the cannula and nostrils, a mask sealed around the face was worn over the cannula and connected to a TSI-4040 flow meter that exhausted to the atmosphere. NHF and facemask flow rates were measured simultaneously to yield lung inspiration and expiration flow rates for cannula flows over a 10–50 l/min range in increments of 10 l/min. Flow rate measurements were also taken without NHF to measure unassisted breathing patterns. The subject was relaxed during measurements. Although the nasal cavity geometry and in vivo flow rates were obtained from different healthy adult males, Tobin et al. (1983) measured the breathing pattern of 65 normal subjects from 20 to 81 years of age and found no effect of age on the mean values of various breathing pattern components or any significant correlation with body height.

The weight and height of the 44-year-old male subject were not available; however, a head circumference of 57 cm was measured from the CT scan data, which compared well with the in vivo subject's head circumference of 58 cm. Both subjects were assumed to be sufficiently similar for any differences in their breathing patterns to fall within a normal range of interpersonal variability (Tobin et al. 1983). Peak flow rates were chosen for investigations because maximum and minimum airway pressures are key measures to breathing therapy and occur at peak expiration and inspiration, respectively, during steady conditions. The peak in vivo flow rates averaged over 5 breaths used in experiments are given in Table 1. Dimensionally similar in vitro flow rates were obtained by matching the Reynolds number in the nasopharynx by Eq. 1.

$$Q_{\text{in-vitro}} = 1.55 \frac{\upsilon_{\text{in-vitro}}}{\upsilon_{\text{in-vivo}}} Q_{\text{in-vivo}} \qquad (1)$$

At the time, a temperature control unit was not available and the working liquid was allowed to vary over a 25–35°C temperature range. The temperature was, however, assumed to be constant for each measurement because the temperature increased by 1°C every 15 min due to the heat generated by the pumps and the measurement period was only 20 s. The temperature was constantly monitored, and between measurements, the flow rate was adjusted based on the viscosity at the time. The dynamic viscosity of the mixture was measured using a Haake RV20/RC20 viscometer and varied linearly from 9.0×10^{-3} Pas at 25°C to 6.8×10^{-3} Pas at 35°C. Over the working temperature

Table 1 In vivo and in vitro flow rates dimensionally scaled by the Reynolds number in the nasopharynx

	In vivo peak flow rate (l/min)		Re in the nasopharynx		In vitro peak flow rate at 25°C (l/min)	
	Inspiration	Expiration	Inspiration	Expiration	Inspiration	Expiration
Unassisted breathing	22	32	1,530	2,230	15.3	22.3
30 l/min cannula	34	18	2,360	1,250	23.7	12.5

range, the density and refractive index variations of 0.35 and 1.4%, respectively, were deemed insignificant. At 25°C, the density was 1,154 kg/m^3 and the refractive index was 1.422.

Breathing is a cyclical process that can be investigated using steady flows based on a quasi-steady approximation (Doorly et al. 2008). For quiet breathing and a respiratory rate of 15 breaths per minute, the Womersley number (W) is 2.5, based on the hydraulic diameter (D_H) of the nasopharynx (Eq. 2). The time scale of a breath is therefore sufficiently long that inertial effects on the flow pattern are negligible and quasi-steady flow can be assumed. The preliminary in vivo breathing flow rate measurements also showed that breath period increased proportionally with increasing cannula flow, reducing the Womersley number. Quasi-steady flow was therefore assumed to hold true with NHF. The increase in breath period with cannula flow is largely due to the increased resistance and duration of expiration. Expiration is a passive process, and the relaxation of the lungs produces a lower peak expiration flow rate with the added resistance of NHF.

$$W = \frac{D_H}{2}\sqrt{\frac{\omega\rho}{\mu}} \qquad (2)$$

2.3 Stereo-PIV cross-correlation algorithm

This section presents an overview of the stereo-PIV cross-correlation (SPIVCC) algorithm developed (Buchmann 2010) and employed in the current study. Parts of the algorithm are developed in C++ language (i.e. cross-correlation, image interpolation) and the overall implementation conducted in Matlab (Mathworks Inc. 2009). A flow chart of the SPIVCC is illustrated in Fig. 6 and briefly described below.

The stereo-PIV system involves the simultaneous acquisition of particle images from each stereocamera. Images are first preprocessed to enhance particle image contrast and reduce image noise, involving background subtraction, low- and high-pass filtering, intensity stretching and thresholding (Honkanen and Nobach 2005; Stitou and Reithmuller 2001; Raffel et al. 1998; Westerweel 1993). The two-dimensional, two velocity components (2D-2C) vector fields are computed separately for each camera and the two-dimensional, three velocity components (2D-3C) velocity field subsequently obtained by stereo-reconstruction.

An in situ three-dimensional calibration-based reconstruction method similar to that described by Soloff et al. (1997) is implemented. This technique does not rely on an accurate knowledge of the geometry of the stereocamera set-up and is able to account for any known and unknown distortion encountered in the real experiment. The cameras

are calibrated on a rectangular calibration grid, which is traversed through the measurement volume at a minimum of three different z locations. The locations of the calibration markers are identified via local pattern matching (i.e. cross-correlation) and used to calculate the coefficients of an image space mapping function by least squares. According to Soloff et al. (1997), a third-order polynomial mapping function is sufficient to account for linear distortions. Others references (see Prasad (2000) for more detail) have used higher orders that have found little or no significant increase in the accuracy of the reconstructed velocity field.

A user-defined regular grid in object space is projected onto each camera such that the resulting vectors are located at the desired object space positions. Typically, a grid spacing that provides an effective interrogation window overlapping factor of 0.5 is applied to increase the spatial sampling. The iterative multigrid analysis consists of a FFT cross-correlation with a two-dimensional Gaussian peak estimator. Optional correlation enhancement methods, such as the correlation-based correction (Hart 2000) or ensemble correlation averaging, are applied (Meinhart et al. 2000). The resulting displacement field is validated using the signal to mean ratio (SMR) and normalised median test (NMT) (typically SMR $\geq$ 1:5, NMT $\geq$ 2). Erroneous vectors are subsequently replaced using a bilinear interpolation and the resulting velocity field is low-pass filtered with a 3 × 3 kernel. Following the first iteration, the predictor field is obtained by bilinear interpolation of the estimated displacement field onto the next higher resolution level. Discrete or fractional window shifting and window deformation techniques (Huang et al. 1993; Scarano 2002; Scarano and Riethmuller 2000) have also been implemented. Image interpolation at sub-pixel locations is performed via the cardinal interpolation function (Scarano 2000). Both cameras are interrogated until the final resolution is achieved.

The 2D-3C reconstruction is performed via a system of linear equations (Soloff et al. 1997) that relate the measured velocity fields in image space to the three-component velocity field in object space. The reconstruction method assumes that the calibration target is aligned with the centre of the light sheet plane. In practice, however, this alignment is difficult and a slight out-of-plane shift or rotation can introduce significant errors in the image to object mapping (Willert 1997; Wieneke 2005). A method for the alignment correction as proposed by Wieneke (2005) is also implemented into the current stereo-PIV procedure. This is generally referred to as self-calibration and shown in Fig. 5 as disparity correction.

The performance and accuracy of the stereo-PIV apparatus and software was assessed using a simple solid body translation experiment that involved the recording of a

Fig. 6 SPIVCC algorithm: flow chart for stereo-PIV vector calculation
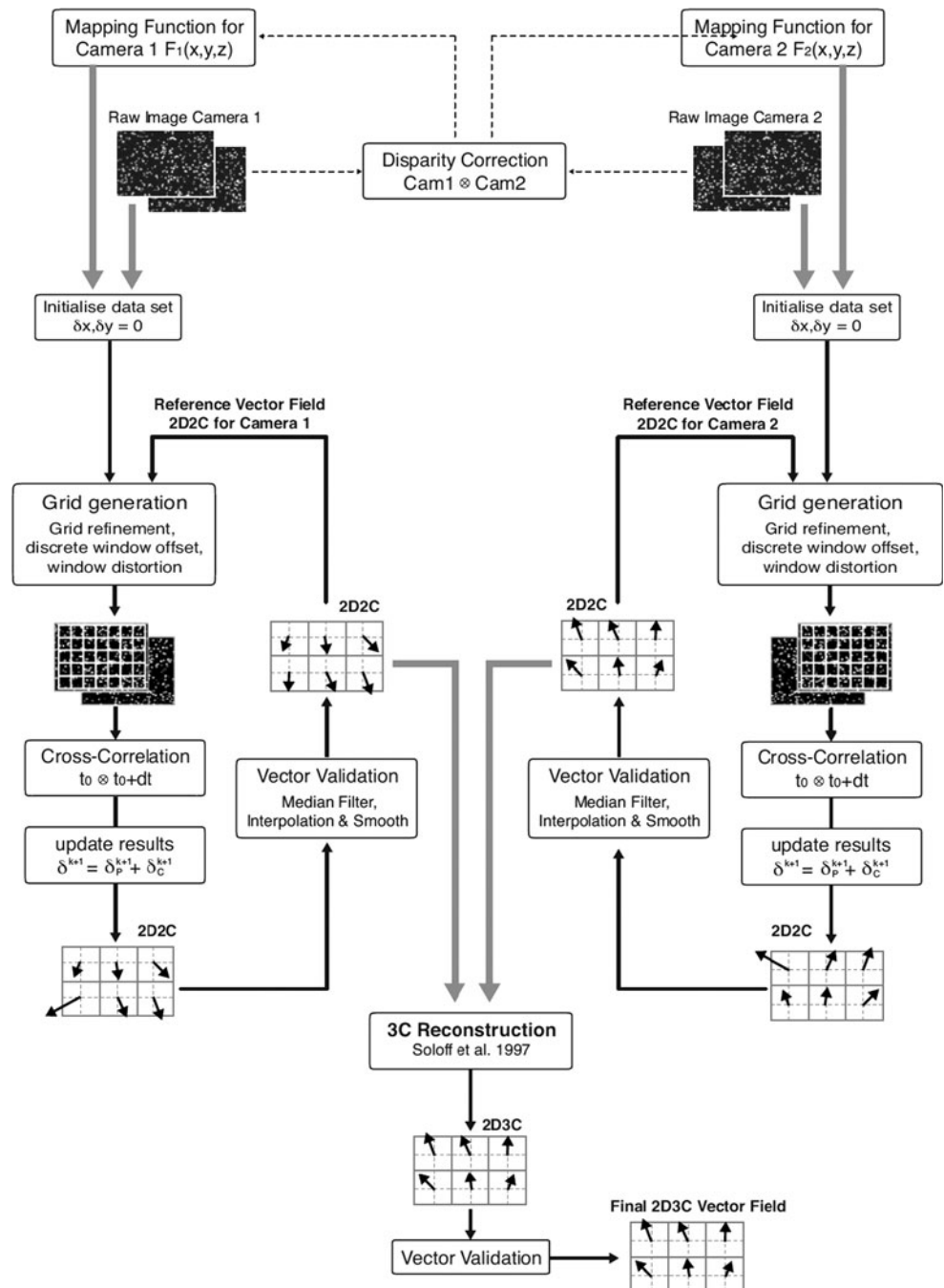
particle image pattern with known displacements and subsequent analysis the SPIVCC algorithm. Seeding particles were simulated by a sheet of 150 grit sandpaper and illuminated with diffused light to provide excellent contrast and signal to noise. The cameras were separated by 90° symmetrically and an acrylic panel placed between the cameras and the object plane to simulate optical distortion similar to that of the real experiment. The particle pattern was displaced by 1 mm ± 5 μm in the x and z directions (i.e. 13–14 pix) with a micrometer driven traverse. The displacement field was computed using a 64 × 64 pix

interrogation window with a 50% overlap and no vector validation.

The statistical results from the resolved displacement in the three principle directions are shown in Table 2. The mean and RMS errors are calculated from a total of 10 measurements and averaged over the entire measurement plane ($N = 5,400$). The RMS error in the x, y and z displacement is a function of the direction of motion and includes the PIV displacement error, interpolation errors, camera calibration errors, target grid spacing errors and traversing errors. For the 1-mm displacement, the

Table 2 Resolved displacements for the three independent traverses investigated

Traversed displacements	Resolved displacements					
	Mean (μm)			RMS (μm)		
	Δx	Δy	Δz	Δx	Δy	Δz
0 mm	0.28	0.25	0.32	0.36	0.29	0.42
1 mm in x	999.2	1.5	5.2	3.1	1.2	4.2
1 mm in z	1.6	1.5	997.2	2.1	1.9	2.2

measurement results show a total error of 0.4 and 0.5% or 3.9 and 5 μm in the x and z directions, respectively. The errors due to a displacement in y direction were not assessed, which are typically of the same order as the x direction (Willert 1997). The ratio between in-plane and out-of-plane error was approximately one and consistent with the theoretical $1/\tan(\alpha)$ relation (Lawson and Wu 1997). The RMS errors for Δx, Δy and Δz are low for the 0-mm displacement and range between 1.2 and 3.1 μm in the case of the 1-mm displacement.

2.4 PIV measurements

The SPIV system used consisted of a 15-Hz dual-head 120 mJ Nd:YAG laser (New Wave Solo XT), two digital 2 mega pixel CCD cameras (Dantec Flowsense) and optics to form a light sheet of approximately 2 mm thickness. The working liquid was seeded with neutrally buoyant 10-μm hollow glass spheres, and sequential images of the illuminated particles were recorded on $1,600 \times 1,200$ pix^2 frames at 10 Hz. Artificial background images were generated by averaging 200 sequential particle images, which were subsequently subtracted from each recording. Non-flow regions were masked to impose a zero flow condition at the fluid–wall interface and to suppress wall reflections. Flow domain cross sections at the various measurement planes were obtained using a CT scan of the flow phantom and the freeware application Paraview (http://www.paraview.org/), enabling the production of accurate mask images.

The particle images were divided into 64×64 pix^2 interrogation regions and the area average displacement calculated by locally cross-correlating the particle image intensities between two subsequent recordings. A grid spacing of 0.6 mm was used, giving an average overlapping factor of 75%, and iterative window refinement was applied with a final interrogation window size of 16×16 pix^2. Window displacement and deformation based on the local velocity gradient was also applied. Displacement fields from 100 image pairs were ensemble averaged to yield mean velocity fields. Although 200 image pairs were captured at each measurement plane, to reduce

computational time and because no appreciable differences in velocities were observed, only 100 image pairs were cross-correlated.

A submersible pump was placed inside the main reservoir to agitate the flow and maintain a seeding concentration as uniform as possible; however, low seeding concentrations due to limited convective mixing and deposition in low velocity regions of the nasal cavity, such as the meatus, necessitated the preprocessing of the raw SPIV images. The seeding concentration was artificially increased by over-sampling 5 images, i.e. adding 5 images together, effectively increasing the seeding density by a factor of 5. Pixel intensities below 5 (8 bit images) were not added to limit the accumulation of noise.

The laser sheet and cameras were fixed, and the reservoir and phantom were traversed to measure 21 sagittal slices through both sides of the cavity at 2.5-mm increments. A sagittal laser plane was anticipated to contain the highest two velocity components and was therefore used to minimise the loss of seeding particles. The maximum velocity for each traversed measurement plane was unique and required time delays ranging between 80 and 1,900 μs to maintain a maximum in-plane displacement of approximately 10 pixels. Although the distance between the cameras and laser plane was constant, the distance between the 8-mm-thick acrylic reservoir wall, which had a refractive index 0.7 above the liquid, and the cameras, which viewed through the distorting medium at an angle without the use of viewing prisms (Prasad and Jensen 1995), was unique for each traverse. The optical distortion from the reservoir wall was therefore unique for each traverse, requiring discrete camera calibrations. Three calibration images were taken at 1-mm spacing for each camera and traverse on a target plate that had 2.5-mm-diameter white dots at 5-mm spacing ($\sim 1,500$ dots). Each dot was least squares mapped to a third-order polynomial (Soloff et al. 1997) typically within an accuracy of 0.5
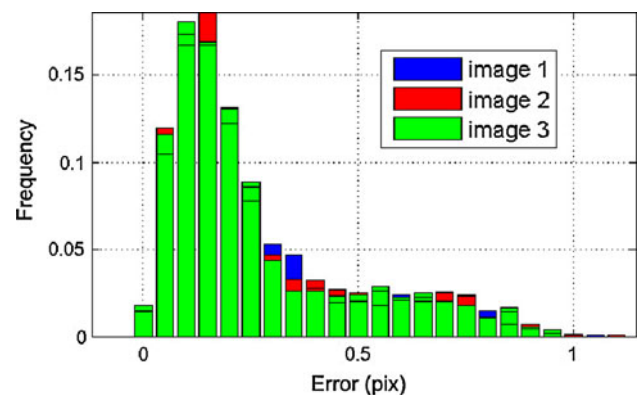
Fig. 7 Histogram showing the calibration error of *each dot*

pixels as shown in Fig. 7 (i.e. mapping error). The cameras were separated by 43.8° and had an average magnification of 0.145 mm/pix. Self-calibrations were performed to correct for small misalignments of the target plate with the laser sheet.

Presented in this paper are SPIV measurements taken at peak expiration and inspiration flows, simulating both ordinary breathing and breathing with cannula flow rates of 30 l/min.

3 Results and discussions

The series of traversed 2D-3C velocity maps obtained were time averaged and reconstructed into a three-dimensional, three velocity components (3D-3C) volume (Fig. 8) using a kriging algorithm (Davis 1986). All velocities shown are in vivo scaled and where applicable, only every fifth vector is displayed for clarity. The average velocity through a cross
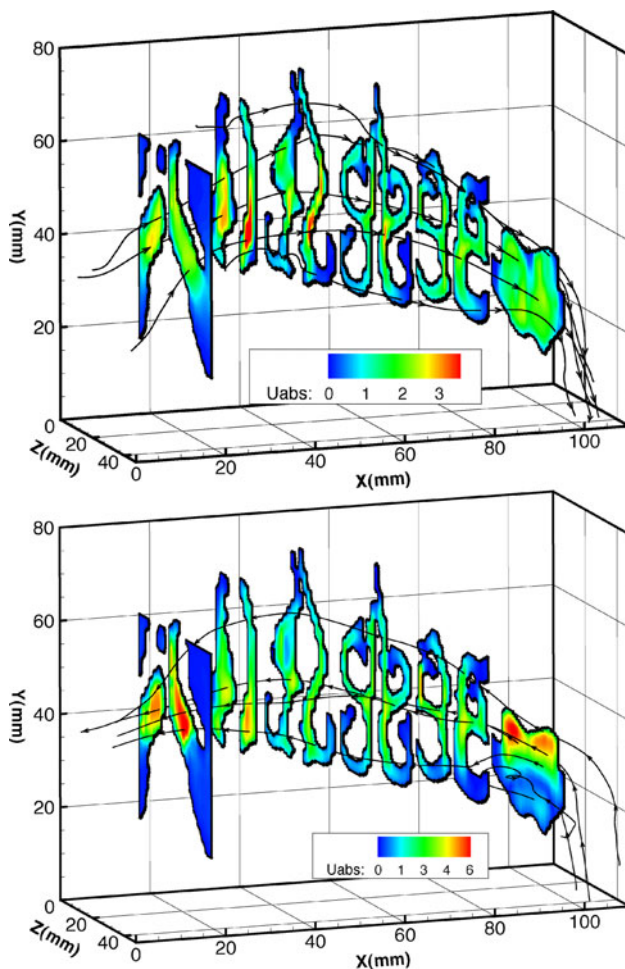

Fig. 8 Coronal cross sections showing the reconstructed 3D velocity field and in vivo scaled absolute velocities (ms^{-1}) on **a** inspiration and **b** expiration

section of the nasopharynx with measured area was obtained to calculate the average flow rate and confirm correct in vivo scaling by achieving the prescribed system flow rate. The vector lengths denote in-plane velocity magnitude and unless stated otherwise the colour contour shows absolute velocity calculated from all three components. For clarity, each figure uses an independent colour contour. Figures 8, 9 and 11 are velocity maps through one sagittal cross section of the left nasal cavity that bisects the nostril. Velocities over 10 and 13 ms^{-1} in Figs. 9b and 11b, respectively, have been omitted to enhance the visualisation of lower velocities.

3.1 Unassisted breathing

Figure 8 shows the distribution of velocities throughout the nasal cavity for unassisted inspiration and expiration. For both conditions, the maximum velocity was located in the small cross-sectional area of the nasal valve. Maximum velocities of 3.1 and 4.2 ms^{-1} were obtained in the left and right nasal valves, respectively, on inspiration and 5.5 and 6.4 ms^{-1} on expiration. The highest velocities occurred in the slightly larger right nasal valve, revealing a bias of flow through the right nasal cavity. Both nasal cavities were exposed to the same inlet and outlet pressures, so the cumulative resistance of the left nasal cavity must have been higher. There are three notable explanations for the higher resistance in the left nasal cavity. First, the smaller cross-sectional area of the left nasal valve poses a greater resistance. Secondly, Fig. 2 shows a rapid expansion into the main cavity following the left nasal valve and a much more gradual gradient for the right. On inspiration, this rapid expansion created a separation region that is prominent in Fig. 9a and is visibly larger in the left nasal cavity in the second anterior cross section of Fig. 8a. The pressure loss associated with this flow separation is therefore larger in the left nasal cavity. The rapid change in cross-sectional area in the left nasal cavity will also create a higher resistance on expiration, however, to a lesser extent due to the favourable pressure gradient. The difference in maximum velocity between the left and right cavity on expiration is indeed less. Thirdly, the smaller cross-sectional area and similar surface area in the left nasal cavity 4.6–8.2 cm from the nostrils create greater levels of viscous shear.

Common to both inspiration and expiration were low flows in the inferior meatus and olfactory region as well as a large proportion of flow passing through the middle airway and along the nasal septum. On expiration (Fig. 9b), a high velocity region on the nasopharynx roof reached 6.4 ms^{-1} as the fast flow rising vertically from the constriction (location 8 in Fig. 2) concentrated on the outside of the near right angle bend from the laryngopharynx. The
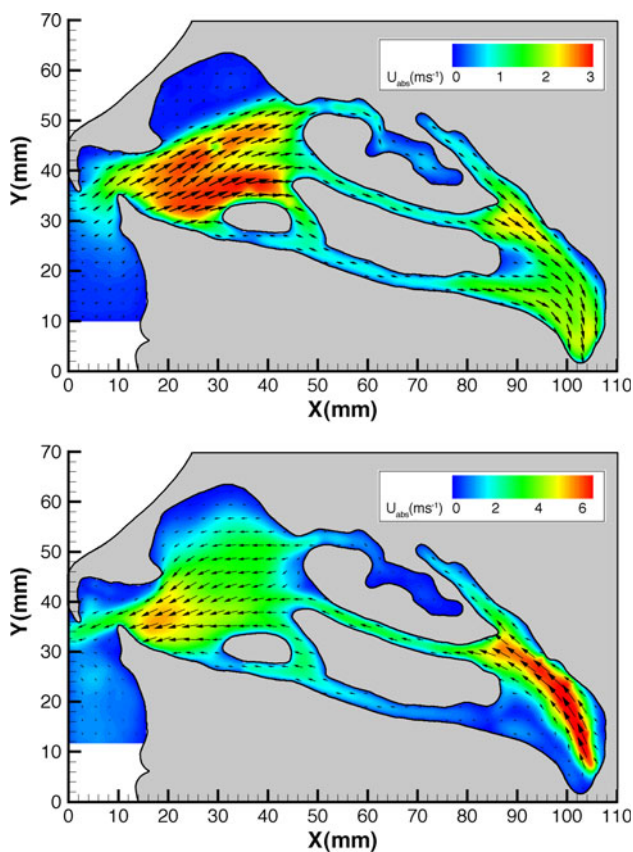
Fig. 9 Velocity maps through one sagittal cross section of the *left* nasal cavity during unassisted breathing on **a** inspiration and **b** expiration

Fig. 10 Orthogonal velocity component contour during unassisted **a** inspiration and **b** expiration (velocities are positive into the page)

subsequent low velocity region on the nasopharynx floor recirculates due to viscous shear from the superior flow stream. The expired flow tends to stay high through the nasal cavity with most of the flow passing through the middle airway and along the nasal septum. In contrast, the flow through the nasopharynx and main cavity on inspiration is vertically distributed more evenly. Air is drawn into the nostrils from wide angles on inspiration and is expired as a horizontal stream of air.

Figure 10 shows the out-of-plane velocity component as the colourmap with positive velocities out of the page. It can be seen that the out-of-plane velocities in the nasal valve make a significant contribution to the absolute velocities up to 36%. On inspiration (Fig. 10a), the flow in the nasal valve points into the page towards the nasal septum and middle airway where the majority of the flow passes. Similarly, on expiration (Fig. 10b), the flow returns to the nasal valve along a comparable vector with some secondary flow visible. It can be seen that the out-of-plane component is small in the narrow meatus as they tend to laminate the flow (Churchill et al. 2004). Velocities in the lateral direction are, however, generally the smallest
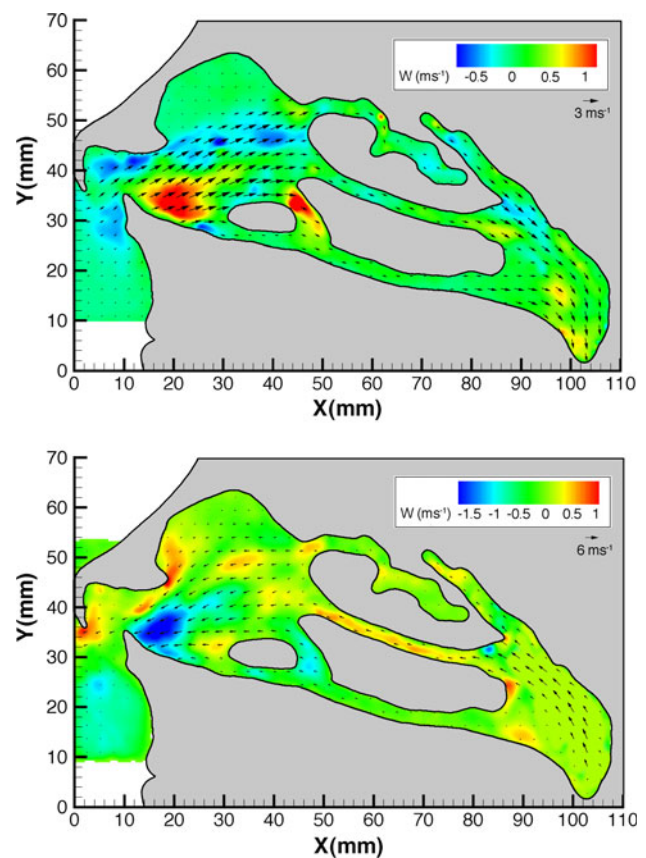
component, and a sagittal laser plane should indeed be used to minimise the loss of seeding particles.

3.2 Unassisted breathing and NHF

Inspiration results obtained with a cannula flow rate of 30 l/min are shown in Fig. 11. During unassisted breathing (Fig. 9a), an eddy is evident superior of the flow separation caused by the abrupt expansion into the nasal cavity, agreeing with results in the literature (Hopkins et al. 2000). The cannula jet strengthened this eddy and a predominant recirculating feature also occurred below the jet. With the cannula resting on the upper lip, the angle and location of the prongs was such that the main flow stream remained towards the cavity roof at same angle as with unassisted inspiration. Inspired flow with NHF is, however, more concentrated on this upwards path and exits the nasal cavity attached to the nasopharynx roof. For a single prong area and flow rate of 19 mm^2 and 15 l/min (30 l/min total cannula flow rate), the theoretical average velocity across the prong is 13.2 ms^{-1}. The maximum measured velocity in the jet was 17.0 ms^{-1}. Figure 12 shows that little flow passes through the inferior
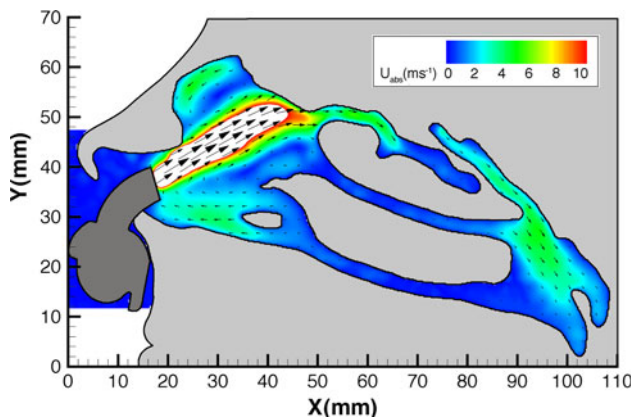
Fig. 11 Velocity map through one sagittal cross section of the *left* nasal cavity during inspiration with 30 l/min cannula flow
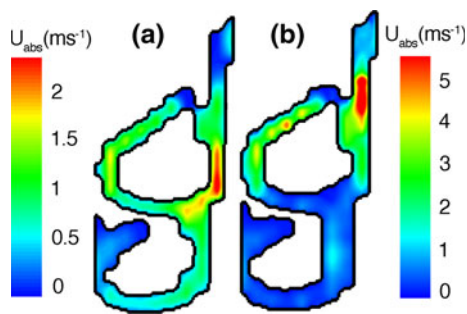

Fig. 12 Coronal cross section of the nasal cavity on inspiration during **a** unassisted breathing and **b** with 30 l/min cannula flow
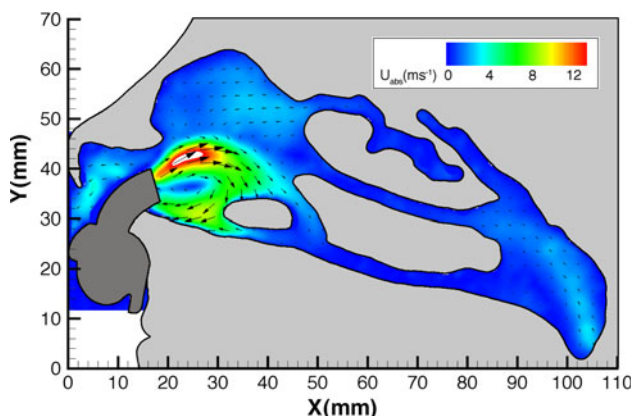

Fig. 13 Velocity map through one sagittal cross section of the *left* nasal cavity during expiration with 30 l/min cannula flow

airway and meatus when compared to unassisted inspiration, and the majority of the flow remains high through the nasal cavity. The maximum velocities in the nasopharynx with and without NHF were 4.3 and 2.6 ms^{-1}, respectively.

Figure 13 shows the expiration results obtained with a cannula flow rate of 30 l/min. With NHF, high velocities were concentrated in the nasal valve and nasal vestibule, where cannula flow was forced to turn 180 degrees by the
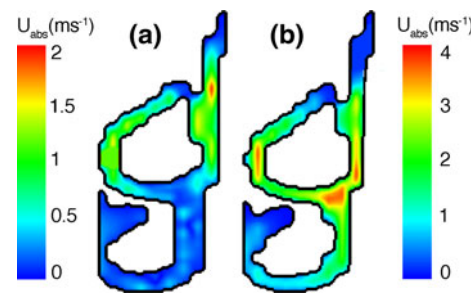

Fig. 14 Coronal cross section of the nasal cavity on expiration during **a** unassisted breathing and **b** with 30 l/min cannula flow

expired volume to additionally exit through the area available between the cannula prong and nostril. The maximum absolute velocity measured was 14.8 ms^{-1}. The momentum required to turn the jet, narrowness of the passageways, large velocity gradients creating high shear and low evenly distributed velocities upstream suggest there is a large pressure drop across the nasal valve with NHF. This resistance is thought to be largely responsible for the elevated airway pressures experienced clinically. Two recirculating features are created with NHF, one clearly in the centre of the jet's retreat and one above the jet in the middle airway. Flow in the nasopharynx is largely unmodified by NHF, with flow remaining attached to the nasopharynx roof. Note that the velocities in the nasopharynx are lower with NHF because peak expiration flow rate is lower and expiration time is longer.

The flow distribution is more evenly distributed vertically through the nasal cavity on expiration with NHF, as shown by Fig. 14. In contrast, the flow during unassisted expiration tends to stay higher through the nasal cavity after entering attached to the nasopharynx roof. The more even distribution of flow through each meatus with NHF is thought to be because of the increased back pressure required to overcome the large resistance created downstream in the nasal cavity anterior and the subsequent relatively small difference in resistance of each upstream passage.

On both inspiration and expiration with NHF, there is a low velocity and recirculation region on the nasopharynx floor. This feature was present on unassisted expiration and was accentuated with NHF, which is a modification to the unassisted inspiration flow pattern. Thinner boundary layers through the nasal valve and meatus are visible in Figs. 11 and 13, indicating increased shear stress and therefore increased flow resistance and moisture and heat transfer in these regions.

4 Conclusions

SPIV was used to measure the flow field in the human nasal cavity during unassisted breathing conditions and with

nasal high flow (NHF) therapy. Physiologically accurate flow rates were measured in vivo and applied in vitro using Reynolds number matching. An anatomically accurate transparent silicone flow phantom including both sides of the nasal cavity was created from CT images. Unassisted breathing inspiration and expiration maximal velocities of 4.2 and 6.4 ms^{-1}, respectively, were located in the nasal valve.

NHF modifies the flow velocity magnitude and distribution in the nasal cavity significantly, altering the proportion of inspiration and expiration through each meatus and producing jet velocities up to 17.0 ms^{-1} for 30 l/min cannula flow. Inspired flow with NHF remains high through the nasal cavity and to a lesser extent so too does expired flow during unassisted breathing. Inspired flow during unassisted breathing and expired flow with NHF are relatively evenly distributed with the main flow stream passing through the middle airway. Strong recirculating features are created above and below the cannula jet on expiration and significantly strengthened on inspiration. Peak inspiration flow rate had a positive relationship with cannula flow rate. Peak expiration flow rate was lower with NHF, which was independent of cannula flow rate.

Velocity magnitudes differed appreciably between the left and right sides of the nasal cavity. During unassisted breathing, the maximum velocity was 39% larger in the right side on inspiration and 18% higher on expiration. Important contributions to flow resistance through the nasal cavity of features other than the nasal valve have been highlighted. Although the morphology was asymmetric about the nasal septum, the flow tended to behave similarly through the features common to both sides of the nasal cavity.

The flow pattern through the nasal cavity is largely two-dimensional; however, lateral velocities have been found to contribute up to 36% of the absolute velocity magnitude in anterior regions. To capture the complete velocity magnitude, a three-component measurement technique such as SPIV or discrete measurement planes aligned parallel to the flow in the nasal cavity anterior with a two-component measurement technique should therefore be used. The highest velocities are located in the sagittal plane; thus, a sagittal light sheet SPIV configuration should be used, as in this study, to minimise the loss of seeding particles.

References

Buchmann NA (2010) Development of particle image velocimetry for in vitro studies of arterial haemodynamics. PhD thesis, University of Canterbury, Christchurch, New Zealand

Çakmak O, Coşkun M, Çelik H, Büyüklü F, Özlüoglu LN (2003) Value of acoustic rhinometry for measuring nasal valve area. Laryngoscope 113:295–302

Campbell EJ, Baker MD, Critessilver P (1988) Subjective effects of humidification of oxygen for delivery by nasal cannula—a prospective-study. Chest 93:289–293

Churchill SE, Shackelford LL, Georgi JN, Black MT (2004) Morphological variation and airflow dynamics in the human nose. Am J Hum Biol 16:625–638

Cole P (2000) Biophysics of nasal airflow: a review. Am J Rhinol 14:245–249

Conway JH, Fleming JS, Perring S, Holgate ST (1992) Humidification as an adjunct to chest physiotherapy in aiding tracheobronchial clearance in patients with bronchiectasis. Respir Med 86:109–114

Davis JC (1986) Statistics and data analysis in geology, 2nd edn. Wiley, New York

Doorly DJ, Taylor DJ, Schroter RC (2008) Mechanics of airflow in the human nasal airways. Respir Physiol Neurobiol 163:100–110

Gibson RL, Comer PB, Beckham RW, McGraw CP (1976) Actual tracheal oxygen concentrations with commonly used oxygen equipment. Anesthesiology 44:71–73

Groves N, Tobin A (2007) High flow nasal oxygen generates positive airway pressure in adult volunteers. Aust Crit Care 20:126–131

Hart D (2000) Super-resolution piv by recursive local-correlation. J Vis 3:187–194

Honkanen M, Nobach H (2005) Background extraction from double-frame PIV images. Exp Fluids 38:348–362

Hopkins LM, Kelly JT, Wexler AS, Prasad AK (2000) Particle image velocimetry measurements in complex geometries. Exp Fluids 29:91–95

Huang HT, Fiedler HE, Wang JJ (1993) Limitation and improvement of piv partii. Exp Fluids 15:263–273

Kelly JT, Prasad AK, Wexler AS (2000) Detailed flow patterns in the nasal cavity. J Appl Physiol 89:323–337

Kim JK, Yoon JH, Kim CH, Nam TW, Shim DB, Shin HA (2006) Particle image velocimetry measurements for the study of nasal airflow. Acta Oto-Laryngol 126:282–287

Lawson NJ, Wu J (1997) Three-dimensional particle image velocimetry: Error analysis of stereoscopic techniques. Meas Sci Technol 8:894–900

Liu Y, Johnson MR, Matida EA, Kherani S, Marsan J (2009) Creation of a standardized geometry of the human nasal cavity. J Appl Physiol 106:784–795

Locke RG, Wolfson MR, Shaffer TH, Rubenstein SD (1993) Inadvertent administration of positive end-distending pressure during nasal cannula flow. Pediatrics 91:135–138

Lund J, Holm-Knudsen RJ, Nielsen J, PB FJ (1996) Nasal cannula versus Hudson face mask in oxygen therapy. J Dan Med Assoc 158(28):4077–4079

Meinhart CD, Wereley ST, Santiago JG (2000) A PIV algorithm for estimating time-average velocity fields. J Fluids Eng 122:285–289

Prasad AK (2000) Stereoscopic particle image velocimetry. Exp Fluids 29:103–116

Prasad AK, Jensen K (1995) Scheimpflug stereocamera for particle image velocimetry in liquid flows. Appl Optics 34(30):7092–7099

Raffel M, Willert CE, Kompenhans J (1998) Particle image velocimetry—a practical guide. Springer, Berlin

Scarano F (2000) Particle image velocimetry and application—investigation of coherent structures in turbulent shear flows. PhD thesis: von Karman Institute for Fluid Dynamics, Universita degli Napoli "Federico II"

Scarano F (2002) Iterative image deformation methods in PIV. Meas Sci Technol 13:R1–R19

Scarano F, Riethmuller ML (2000) Advances in iterative multigrid PIV image processing. Exp Fluids 29:S51–S60

Soloff SM, Adrian RJ, Liu ZC (1997) Distortion compensation for generalized stereoscopic particle image velocimetry. Meas Sci Technol 8:1441–1454

Sreenan C, Lemke RP, Hudson-Mason A, Osiovich H (2001) High-flow nasal cannulae in the management of apnea of prematurity: a comparison with conventional nasal continuous positive airway pressure. Pediatrics 107:1081–1083

Stitou A, Reithmuller ML (2001) Extension of PIV to super resolution using PTV. Meas Sci Technol 12:1398–1403

Tobin MJ, Chadha TS, Jenouri G, Birch SJ, Gazeroglu HB, Sackner MA (1983) Breathing patterns: 1. Normal subjects. Chest 84:202–206

Westerweel J (1993) Digital particle image velocimetry—theory and application. PhD thesis, Delft University, Delft, Netherlands

Wieneke B (2005) Stereo-PIV using self-calibration on particle images. Exp Fluids 39:267–280

Willert C (1997) Stereoscopic digital particle image velocimetry for application in wind tunnel flows. Meas Sci Technol 8:1465–1479

William EL, Harvey EC (1987) Marching cubes: a high resolution 3D surface construction algorithm. SIGGRAPH Comput Graph 21:163–169

Wolf M, Naftali S, Schroter RC, Elad D (2004) Air-conditioning characteristics of the human nose. J Laryngol Otol 118:87–92